

# A systematic analysis of parametric instabilities in nonlinear parabolic multimode fibers

Cite as: APL Photonics 4, 022803 (2019); doi: 10.1063/1.5044659

Submitted: 14 June 2018 • Accepted: 2 October 2018 •

Published Online: 13 December 2018



H. E. Lopez-Aviles,<sup>1,a)</sup> F. O. Wu,<sup>1</sup> Z. Sanjabi Eznaveh,<sup>1</sup> M. A. Eftekhar,<sup>1</sup> F. Wise,<sup>2</sup> R. Amezcua Correa,<sup>1</sup> and D. N. Christodoulides<sup>1</sup>

## AFFILIATIONS

<sup>1</sup>CREOL, The College of Optics and Photonics, University of Central Florida, Orlando, Florida 32816, USA

<sup>2</sup>School of Applied and Engineering Physics, Cornell University, Ithaca, New York 14853, USA

<sup>a)</sup>h.lopez@knights.ucf.edu

## ABSTRACT

We provide a systematic analysis of geometric parametric instabilities in nonlinear graded-index multimode fibers. Our approach implicitly accounts for self-focusing effects and considers dispersion processes to all orders. It is shown that the resulting parametric problem takes the form of a Hill's equation that can be systematically addressed using a Floquet approach. The theory developed indicates that the unstable spectral domains associated with such geometric parametric instabilities can be significantly altered as the power levels injected in a parabolic multimode fiber increase. These predictions are in excellent agreement with experimental data gathered from graded-index multimode structures.

© 2018 Author(s). All article content, except where otherwise noted, is licensed under a Creative Commons Attribution (CC BY) license (<http://creativecommons.org/licenses/by/4.0/>). <https://doi.org/10.1063/1.5044659>

## I. INTRODUCTION

For decades, the landscape of fiber optic technologies has been dominated by single-mode fibers (SMFs). Monomode optical waveguide structures have been successfully used not only in telecommunications but also in a variety of nonlinear optical settings.<sup>1–10</sup> The emergence of photonic crystal fibers and the prospect of controlling at will their dispersion characteristics have further enriched the field of nonlinear fiber optics.<sup>11,12</sup> In the last few years, there has been a resurgence of interest in deploying multimode fibers (MMFs) as a means of enhancing the bandwidth of telecom systems through the use of space-division multiplexing.<sup>13</sup> Motivated by these developments, the study of nonlinear wave interactions in MMFs has recently received considerable attention.<sup>14–20</sup> In such heavily multimoded nonlinear environments, all the modes involved dynamically interact through the  $\chi^{(3)}$  processes of self-phase and cross-phase modulation, four-wave mixing, and stimulated Raman scattering. In this respect, MMFs can provide a versatile platform to investigate altogether new nonlinear propagation phenomena such as spatiotemporal dynamics,<sup>21–23</sup> spatial beam self-cleaning,<sup>24</sup> rogue waves,<sup>25</sup> and spatiotemporal mode-locking<sup>26</sup> to mention a few. In this respect, graded-index (GRIN) MMFs play

a prominent role due to the fact that the differential group delay between modes can be considerably suppressed.<sup>27,28</sup> In this same parabolic index guiding system, the mode propagation constants happen to be equidistant, and as a result, beam revivals in the form of compressions and expansions periodically occur during propagation, as schematically depicted in Fig. 1. As recently indicated in a number of theoretical and experimental studies, under nonlinear conditions, this natural periodic beam behavior can give rise to a special class of parametric instabilities—better known as geometric parametric instabilities (GPIs).<sup>29,30</sup> Unlike modulational instability, GPI can take place in both the normal and anomalous dispersion regimes. Indeed, as shown in a number of recent studies, the GPI mechanism plays an important role in inciting supercontinuum generation in GRIN MMFs even in the normal dispersion region.<sup>31,32</sup>

In general, nonlinear light propagation in a MMF is a complex problem to analyze since it involves coupled spatial and temporal effects between hundreds or thousands of modes. Along these lines, several numerical studies have been carried out to describe the space-time dynamics in parabolic MMFs based on perturbative schemes.<sup>29</sup> Another avenue in investigating these effects is to describe nonlinear pulse propagation

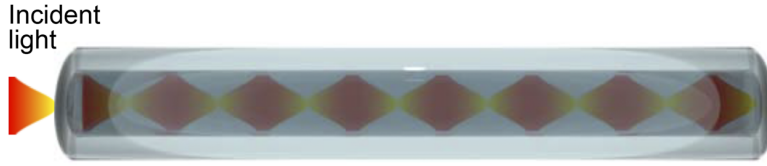


**FIG. 1.** Periodic compressions and expansions of an optical beam in a GRIN MMF, as a consequence of the equidistant distribution of propagation eigenvalues.

in such structures after reducing the (3 + 1)D Gross-Pitaevskii equation into a simpler (1 + 1)D nonlinear Schrödinger equation.<sup>33</sup> Clearly, of interest will be to develop a formalism capable of capturing all the produced GPI sidebands, in both dispersion regimes—including the case where self-focusing revivals in MMFs could be an issue.

In this work, we present a rigorous analysis of GPI effects in MMFs that includes dispersion effects to all orders, while at the same time, it accounts for spatial self-focusing oscillations. Note that under these conditions, a perturbative treatment is no longer valid. To analyze this problem, we employed an exact Floquet scheme as a means to obtain the corresponding stability diagrams and their associated gain spectra for the system under consideration. Analytical results supported by numerical simulations indicate that as the input power is increased, the generated GPI sidebands in GRIN MMFs tend to move closer to the pump wavelength, thus experiencing higher amplification rates.

## II. THEORETICAL ANALYSIS OF GPI

### A. Variational approach

We begin our analysis by expressing the optical electric field propagating in a nonlinear parabolic MMF in the form  $E = \varphi e^{i(kz - \omega_0 t)}$ , where  $\varphi(x, y, z, t)$  represents the field envelope. In this case, the nonlinear dynamical evolution equation governing this envelope takes the form of a generalized nonlinear Schrödinger equation (GNLSE) in the presence of a parabolic potential, i.e.,

$$i \frac{\partial \varphi}{\partial z} + \frac{1}{2k} \nabla_{\perp}^2 \varphi - \frac{k\Delta}{a^2} (x^2 + y^2) \varphi + \sum_{n=2}^{\infty} \frac{i^n \beta_0^{(n)}}{n!} \frac{\partial^n \varphi}{\partial T^n} + k_0 n_2 |\varphi|^2 \varphi = 0. \quad (1)$$

In the above equations,  $k = k_0 n_0$ ,  $k_0 = \omega_0/c$ ,  $n_0$  is the refractive index at the center of the GRIN MMF core,  $\Delta$  is the relative refractive index difference, and  $a$  is the core radius. In addition,  $\beta_0^{(n)} = d^n k / d\omega^n$  denotes the  $n$ th dispersion coefficient evaluated at the carrier frequency  $\omega_0$ ,  $n_2$  stands for the nonlinear Kerr coefficient associated with silica glass, and  $T = t - z/v_g$  represents a time coordinate system that moves at the group speed  $v_g$ . In deriving Eq. (1), we implicitly assumed that all the modes involved in the weakly guiding MMF share the same linear polarization, once they are excited on-center by a linearly polarized Gaussian beam. While our treatment assumes an infinite parabolic profile having an equidistant distribution of propagation eigenvalues, one should also keep in mind the effects arising from a cladded finite size core where this distribution is disturbed for the highest-order modes.

Nevertheless, in both our theory and experiments, we practically assume that only lower-order sets of  $LP_{0m}$  modes are excited, in which case beam oscillations are still expected to take place.

To analyze this problem, we adopt a solution of the form  $\varphi(x, y, z, T) = u(z, T)G(x, y, z)$ , while assuming continuous wave (CW) conditions. In order to investigate the stability of the CW component, we write  $u(z, T) = 1 + \epsilon(z, T)$ , where  $\epsilon(z, T)$  describes a small complex perturbation ( $|\epsilon| \ll 1$ ). For convenience, the amplitude of the background wave was taken here to be unity. Direct substitution of these latter forms in Eq. (1) readily provides the following results:

$$i \frac{\partial G}{\partial z} + \frac{1}{2k} \nabla_{\perp}^2 G - \frac{k\Delta}{a^2} (x^2 + y^2) G + k_0 n_2 |G|^2 G = 0, \quad (2)$$

$$i \frac{\partial \epsilon}{\partial z} G + G \sum_{n=2}^{\infty} \frac{i^n \beta_0^{(n)}}{n!} \frac{\partial^n \epsilon}{\partial T^n} + k_0 n_2 |G|^2 G (\epsilon + \epsilon^*) = 0. \quad (3)$$

In order to eliminate the  $(x, y)$  spatial dependence in Eq. (3), we then multiply all terms with  $G^*(x, y, z)$  and subsequently integrate over the transverse plane. By doing so, we obtain

$$i \frac{\partial \epsilon}{\partial z} + \sum_{n=2}^{\infty} \frac{i^n \beta_0^{(n)}}{n!} \frac{\partial^n \epsilon}{\partial T^n} + k_0 n_2 (\epsilon + \epsilon^*) \frac{\int \int dx dy |G|^4}{\int \int dx dy |G|^2} = 0, \quad (4)$$

where in general, the ratio of the two overlap integrals [the last term of Eq. (4)] can still be a function of  $z$ . Equation (2) can be further treated using a variational approach, along the lines described in Refs. 34 and 35. In this respect, we first normalize Eq. (2) using the dimensionless coordinates  $X = x/\sigma$ ,  $Y = y/\sigma$ , with  $\sigma$  being the spot size of the fundamental mode  $\sigma = (a/k)^{1/2} (2\Delta)^{-1/4}$ . Finally, the longitudinal axis is normalized according to  $\xi = z\sqrt{2\Delta}/a$ . From here, Eq. (2) can be rewritten as

$$i \frac{\partial g}{\partial \xi} + \frac{1}{2} \nabla_{\perp}^2 g - \frac{1}{2} (X^2 + Y^2) g + |g|^2 g = 0, \quad (5)$$

where  $g = \sqrt{\gamma} G$  and  $\gamma = k_0 n_2 a / \sqrt{2\Delta}$  is indicative of the nonlinearity involved. The corresponding Lagrangian density associated with Eq. (5) is given by

$$L(X, Y, \xi) = \frac{i}{2} \left( g \frac{\partial g^*}{\partial \xi} - g^* \frac{\partial g}{\partial \xi} \right) + \frac{1}{2} \left| \frac{\partial g}{\partial X} \right|^2 + \frac{1}{2} \left| \frac{\partial g}{\partial Y} \right|^2 + \frac{1}{2} (X^2 + Y^2) |g|^2 - \frac{1}{2} |g|^4. \quad (6)$$

In what follows, we solve Eq. (5) by adopting a Gaussian ansatz for the spatial beam profile, i.e.,

$$g(X, Y, \xi) = A(\xi) \exp \left[ -\frac{X^2 + Y^2}{2W^2(\xi)} + ib(\xi)(X^2 + Y^2) \right], \quad (7)$$

here,  $A(\xi)$  is a complex field amplitude and  $W(\xi)$  is a normalized beam spot size ( $W = w_a/\sigma$ ), where  $w_a(\xi)$  is the actual spot size (in  $\mu\text{m}$ ) of this CW Gaussian optical beam as a function of distance  $\xi$ . Moreover,  $b(\xi)$  is related to the phase curvature of this same beam.

By substituting Eq. (7) in Eq. (6) and after introducing the reduced Lagrangian density  $\langle L(\xi) \rangle = \int_{-\infty}^{\infty} dXdY L(X, Y, \xi)$ , we obtain the following results, after applying the Euler-Lagrange equations:

$$\frac{d}{d\xi} \left( i \frac{W^2}{4} A \right) = -i \frac{W^2}{4} \frac{dA}{d\xi} + \frac{W^4}{2} A \frac{db}{d\xi} + \frac{A}{2} \left( \frac{1}{2} + 2b^2 W^4 \right) + \frac{W^4}{4} A - \frac{W^2}{4} |A|^2 A, \quad (8)$$

$$\frac{d}{d\xi} \left( -i \frac{W^2}{4} A^* \right) = i \frac{W^2}{4} \frac{dA^*}{d\xi} + \frac{W^4}{2} A^* \frac{db}{d\xi} + \frac{A^*}{2} \left( \frac{1}{2} + 2b^2 W^4 \right) + \frac{W^4}{4} A^* - \frac{W^2}{4} |A|^2 A^*, \quad (9)$$

$$i \frac{W}{2} \left( A \frac{dA^*}{d\xi} - A^* \frac{dA}{d\xi} \right) + 2W^3 |A|^2 \frac{db}{d\xi} + 4|A|^2 b^2 W^3 + W^3 |A|^2 - \frac{W}{4} |A|^4 = 0, \quad (10)$$

$$\frac{d}{d\xi} \left( \frac{W^4}{2} |A|^2 \right) = 2|A|^2 b W^4. \quad (11)$$

By combining Eqs. (8) and (9), we find

$$\frac{d}{d\xi} (|A|^2 W^2) = 0, \quad (12)$$

from where one can deduce the following power conservation law:  $|A|^2 W^2 = |A_0|^2 W_0^2 = C_0^2$ , where  $W_0$  and  $A_0$  are, respectively, the normalized initial spot size and the scaled peak electric field amplitude (associated with  $g(X, Y, \xi)$ ) when the Gaussian beam size is either a maximum or a minimum. In the previous expressions,  $C_0^2$  represents the normalized input power. From Eqs. (8)–(10), we can then derive the following differential equation

$$\frac{db}{d\xi} = \frac{1}{2W^4} - 2b^2 - \frac{1}{2} - \frac{|A|^2}{4W^2}, \quad (13)$$

while from Eqs. (11) and (12), we get

$$\frac{dW}{d\xi} = 2bW. \quad (14)$$

Equations (13) and (14) then directly lead to the following second-order Ermakov<sup>36</sup> differential equation that describes the evolution of the normalized spot size during propagation:

$$\frac{d^2 W}{d\xi^2} = \frac{1}{W^3} \left( 1 - \frac{C_0^2}{2} \right) - W. \quad (15)$$

Equation (15) represents the main result of the variational approach. After a linearization procedure,<sup>36</sup> this Ermakov equation can be directly solved. A particular solution of relevance to the discussion here is given by

$$W^2(\xi) = \frac{W_0^2}{2} [1 + C + (1 - C) \cos(2\xi)], \quad (16)$$

where  $C = 1/W_0^4 - |A_0|^2/2W_0^2$  is a dimensionless parameter that provides a measure as to the relative strengths of diffraction versus self-focusing effects. If  $C > 1$ , diffraction effects dominate, whereas if  $C < 1$ , then self-focusing prevails. In the case where  $C = 1$ , the two processes are balanced and, in principle, can lead to a spatial soliton solution. Equation (16) remarkably shows that the beating frequency in a parabolic MMF does not depend on the power levels used. In other words, even close to self-focusing, the beam oscillation period along  $z$  ( $\hat{z} = \pi a/\sqrt{2\Delta}$ ) remains invariant, exactly as expected from linear conditions.

We note that identical results could have been directly reached from the Virial theorem associated with the (2 + 1)D NLSE, as first obtained by Pitaevskii.<sup>37</sup> In this respect, Eq. (16) can be obtained from the evolution of the second moment under the assumption of a Gaussian ansatz. Beam propagation simulations also support this Gaussian assertion.

## B. Hill's equation

In Sec. II A, we obtained an analytical expression capable of describing the beam spot size during propagation, even in the presence of self-focusing effects. In what follows, we will analyze the temporal stability properties of the CW background, by considering the evolution dynamics of the perturbation  $\epsilon(z, T)$ , as dictated by Eq. (4). Note that under the Gaussian ansatz, the ratio of overlap integrals in Eq. (4) is proportional to the ratio  $W_0^2/W^2(\xi)$ . As a result, the beam oscillations in this parabolic fiber lead to an equivalent nonlinearity that happens to be periodic with propagation distance. It is exactly this cyclic dependence that leads to GPI. By again adopting normalized coordinates and fields  $(X, Y, \xi, g)$ , Eq. (4) takes the scaled form

$$i \frac{\partial \epsilon}{\partial \xi} + \frac{a}{\sqrt{2\Delta}} \sum_{n=2}^{\infty} \frac{i^n \beta_0^{(n)}}{n!} \frac{\partial^n \epsilon}{\partial T^n} + \frac{|A_0|^2 W_0^2}{2W^2(\xi)} (\epsilon + \epsilon^*) = 0. \quad (17)$$

The properties of this latter equation can be investigated by assuming a perturbation having two angular frequency sidebands at  $\pm\Omega$ ,

$$\epsilon(\xi, T) = D_1(\xi) e^{i\Omega T} + D_2(\xi) e^{-i\Omega T}, \quad (18)$$

where  $D_{1,2}(\xi)$  are the corresponding amplitudes. By adopting an approach similar to the one outlined in Ref. 38, Eqs. (17) and (18) can lead to the following two equations:

$$\frac{dD_4}{d\xi} + \frac{a}{\sqrt{2\Delta}} \left[ D_3 \sum_{n=1}^{\infty} \frac{\beta_0^{(2n)}}{(2n)!} \Omega^{(2n)} - D_4 \sum_{n=1}^{\infty} \frac{\beta_0^{(2n+1)}}{(2n+1)!} \Omega^{(2n+1)} \right] + \frac{|A_0|^2 W_0^2}{W^2(\xi)} D_3 = 0, \quad (19)$$

$$\frac{dD_3}{d\xi} + \frac{a}{\sqrt{2\Delta}} \left[ D_4 \sum_{n=1}^{\infty} \frac{\beta_0^{(2n)}}{(2n)!} \Omega^{(2n)} - D_3 \sum_{n=1}^{\infty} \frac{\beta_0^{(2n+1)}}{(2n+1)!} \Omega^{(2n+1)} \right] = 0, \quad (20)$$

where  $D_3(\xi) = D_1(\xi) + D_2^*(\xi)$  and  $D_4(\xi) = D_1(\xi) - D_2^*(\xi)$ . One can directly show that this system can be further reduced to a second-order differential equation for  $D_3(\xi)$ , i.e.,

$$\frac{d^2 D_3}{d\xi^2} + i \frac{2a}{\sqrt{2\Delta}} \beta_{\text{odd}} \frac{dD_3}{d\xi} + \left[ \frac{a^2}{2\Delta} \beta_e^2 - \frac{a^2}{2\Delta} \beta_{\text{odd}}^2 + \frac{a}{\sqrt{2\Delta}} \beta_e \frac{|A_0|^2 W_0^2}{W^2(\xi)} \right] D_3 = 0, \quad (21)$$

where  $\beta_{\text{odd}}(\Omega) \equiv \sum_{n=1}^{\infty} \Omega^{(2n+1)} \beta_0^{(2n+1)} / (2n+1)!$  and  $\beta_e(\Omega) \equiv \sum_{n=1}^{\infty} \Omega^{(2n)} \beta_0^{(2n)} / (2n)!$  are by definition two dispersion functions involving either odd or even terms.

Equation (21) can be subsequently simplified by using a change of variables  $D_3(\xi) = P(\xi) \exp(-ia\beta_{\text{odd}}\xi/\sqrt{2\Delta})$  from where one can obtain a Hill's equation

$$\frac{d^2 P}{d\xi^2} + \frac{a^2}{2\Delta} [\beta_e^2 + \beta_e k_0 n_2 |A_0|^2 W_0^2 f(\xi)] P = 0, \quad (22)$$

where  $f(\xi) = 1/W^2(\xi)$ . Equation (22) describes the dynamics of the GPI sidebands, by taking into account dispersive effects to all orders. We note that higher-order dispersive effects can profoundly alter the stability diagram, to the point that the GPI sidebands expected from only quadratic dispersion can totally disappear, depending on the magnitude and sign of higher-order dispersive terms. In addition, unlike perturbative schemes, our formalism can treat this problem even under high intensity conditions, where the beam spot size revivals can be significantly affected by the power levels involved.

### III. STABILITY ANALYSIS AND GPI GAIN

#### A. Stability diagrams

As previously indicated, Eq. (22) encompasses all the stability properties of the GPI process in a parabolic MMF. This equation is now analyzed using Floquet theory. To do so, one should keep in mind that the Fourier coefficients of the term  $f(\xi)$  in Eq. (22) are given by

$$f(\xi) = \frac{2}{W_0^2 [1 + C + (1 - C) \cos(2\xi)]} = \frac{1}{2} a_0 + \sum_{m=1}^{\infty} a_m \cos(2m\xi), \quad (23)$$

where

$$a_m = \frac{2}{W_0^2 \sqrt{C}} \left( \frac{2\sqrt{C} - 1 - C}{1 - C} \right)^m, \quad m = 0, 1, 2, \dots \quad (24)$$

We emphasize that the coefficients  $a_m$  now depend on the overall power conveyed in this GRIN MMF, as described by the parameter  $C$ . Next, to identify the boundaries (in parameter space) of the stability diagram, we assume periodic solutions of period  $2\pi$ . In other words, the solution of Eq. (22) can be represented by a Fourier series<sup>39,40</sup>

$$P(\xi) = e^{\mu\xi} \sum_{n=-\infty}^{\infty} d_n e^{in\xi}. \quad (25)$$

In this case, to find the boundaries of the stability diagram (separating stable from unstable regions), we will set the exponent to be  $\mu = 0$ . Substitution of Eqs. (23)–(25) in Eq. (22) leads to the following set of homogeneous linear equations:

$$\dots + \frac{\rho}{2} a_2 d_{n-4} + \frac{\rho}{2} a_1 d_{n-2} + \left( \eta + \frac{\rho}{2} a_0 - n^2 \right) d_n + \frac{\rho}{2} a_1 d_{n+2} + \frac{\rho}{2} a_2 d_{n+4} + \dots = 0, \quad (26)$$

where the stability parameters are  $\eta \equiv a^2 \beta_e^2 / 2\Delta$  and  $\rho \equiv a^2 \beta_e k_0 n_2 |A_0|^2 W_0^2 / 2\Delta$ . This set of equations admits non-trivial solutions provided that the determinant formed by the coefficients of  $d_n (n = 0, \pm 1, \pm 2, \dots)$  in Eq. (26) is itself zero,

$$\begin{vmatrix} \vdots & & & & & \\ \eta + \frac{\rho}{2} a_0 - 4 & 0 & \frac{\rho}{2} a_1 & 0 & \frac{\rho}{2} a_2 & \\ 0 & \eta + \frac{\rho}{2} a_0 - 1 & 0 & \frac{\rho}{2} a_1 & 0 & \\ \dots & \frac{\rho}{2} a_1 & 0 & \eta + \frac{\rho}{2} a_0 & 0 & \frac{\rho}{2} a_1 & \dots \\ 0 & \frac{\rho}{2} a_1 & 0 & \eta + \frac{\rho}{2} a_0 - 1 & 0 & \\ \frac{\rho}{2} a_2 & 0 & \frac{\rho}{2} a_1 & 0 & \eta + \frac{\rho}{2} a_0 - 4 & \\ \vdots & & & & & \end{vmatrix} = 0. \quad (27)$$

The stability diagram associated with this Hill's equation can be subsequently extracted by determining the boundaries between stable and unstable regions. This is accomplished by separately solving the determinant of Eq. (27) when the index  $n$  is even or odd, in which case the solutions have a period  $\pi$  or  $2\pi$ , respectively. By merging these solutions, the transition curves (separating stable and unstable regions) can be determined. Even more importantly, the stability dynamics of the Hill's equation (22) are only dictated by the even dispersion function  $\beta_e(\Omega)$ , while the odd  $\beta_{odd}(\Omega)$  is inconsequential for the GPI.

## B. GPI gain spectrum

In Sec. III A, we outlined a systematic procedure with the help of which one can determine the stability diagram boundaries associated with the GPI process. Clearly of importance will be to evaluate the corresponding GPI gain spectra, as dictated by the Hill's equation (22). Evidently, in Eq. (25), the real part of  $\mu$  (only possible in the unstable regions of the GPI diagram) represents a normalized gain coefficient for a specific frequency sideband  $\Omega$ , conveyed in the parameters  $\eta$  and  $\rho$ . By substituting Eq. (25) in (22) and after considering only even terms of the index  $n$ , we obtain the same set of homogeneous equations (26); only this time we assume that  $\mu \neq 0$ , which implies that the coefficient of  $d_n$  in (26) is now instead  $\eta + \rho a_0/2 + (\mu + in)^2$ .

The complex exponent  $\mu$  can then be determined by setting the infinite determinant formed by the coefficients of  $d_n$ , also known as Hill's determinantal, to zero,

$$\begin{vmatrix} \vdots & & & \\ \eta + \frac{\rho}{2}a_0 + (\mu - 2i)^2 & \frac{\rho}{2}a_1 & \frac{\rho}{2}a_2 & \\ \cdots & \frac{\rho}{2}a_1 & \eta + \frac{\rho}{2}a_0 + \mu^2 & \frac{\rho}{2}a_1 & \cdots \\ & \frac{\rho}{2}a_2 & \frac{\rho}{2}a_1 & \eta + \frac{\rho}{2}a_0 + (\mu + 2i)^2 & \\ & \vdots & & & \end{vmatrix} = 0. \quad (28)$$

Surprisingly the roots of the aforementioned Hill's determinantal equation can be analytically obtained through the

following closed form expression:<sup>40</sup>

$$\sin^2\left(\frac{1}{2}\pi i\mu\right) = \Delta(0) \sin^2\left(\frac{1}{2}\pi\sqrt{\eta + \frac{\rho}{2}a_0}\right), \quad (29)$$

where  $\Delta(0)$  is the determinant corresponding to  $\mu = 0$  (at the boundaries of the stability diagram). Using Eq. (29), one can evaluate  $\mu$  as a function of the parameters  $\eta$  and  $\rho$ . In general,  $\mu$  can be complex (in the unstable regions) or purely imaginary (stable regions). As previously indicated, if  $\mu$  happens to be complex, then the corresponding frequency  $\Omega$  will experience gain.

## IV. NONLINEAR PROPAGATION IN GRIN MMF AND EXPERIMENTAL OBSERVATION OF GPI

Based on the results of Secs. II and III, we next analyze the GPI mechanism in actual parabolic MMF settings. For demonstration purposes, in our study, we assume a core radius of  $25\ \mu\text{m}$  and a relative index difference of  $\Delta = (n_0 - n_{\text{clad}})/n_0 \approx 1 \times 10^{-2}$ . The operating wavelength is taken to be  $1064\ \text{nm}$ , and the peak power used ranges from  $30\ \text{kW}$  to  $500\ \text{kW}$ . The actual input spot size of the Gaussian beam injected in the GRIN MMF is here assumed to be  $13.5\ \mu\text{m}$ , and the Kerr coefficient  $n_2 = 1.2 \times 10^{-22}\ \text{m}^2/\text{V}^2$ . Note that in this MMF, the beam undergoes periodic oscillations having a spatial period of  $0.55\ \text{mm}$ . The parameters  $\eta$  and  $\rho$  associated with the stability diagrams are then evaluated based on the even and odd dispersion functions  $\beta_e(\Omega)$  and  $\beta_{odd}(\Omega)$  as obtained from the refractive index Sellmeier expansion associated with silica glass.<sup>41</sup> Using the aforementioned parameters and with the help of Eq. (27), one can then determine the boundaries of the stability diagram for a given input power, by scanning through the coordinates  $\rho$  and  $\eta + \rho$ , as shown in Fig. 2(a). As an example, for the assumed parameters, we here present these diagrams for two different power levels,  $30\ \text{kW}$  (blue curves) and  $500\ \text{kW}$  (red curves). The unstable regions where GPI is possible are shown in yellow. Of course, once the  $\eta, \rho$  parameters are linked through the actual silica Sellmeier expansion, they provide an operational curve as shown by the black and green curves corresponding to  $30$  and  $500\ \text{kW}$ , respectively, in

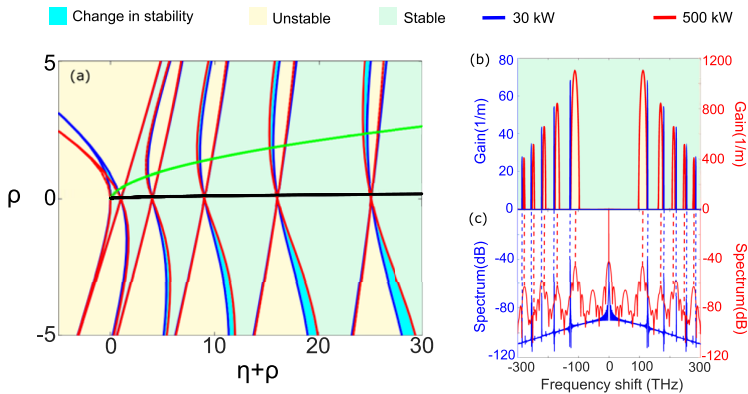


**FIG. 2.** (a) Stability diagrams depicting stable and unstable GPI regions as extracted from the Hill's equation when the input power is  $30\ \text{kW}$  (blue curves) and  $500\ \text{kW}$  (red curves). The black ( $30\ \text{kW}$ ) and green ( $500\ \text{kW}$ ) curves correspond to the operating parameters of our system as the frequency varies. (b) GPI gain spectra associated with the stability diagrams of (a) and (c) GPI sidebands obtained from numerical simulations. The parameters used here are  $\lambda_0 = 1064\ \text{nm}$ ,  $a = 25\ \mu\text{m}$ , and  $w_a = 13.5\ \mu\text{m}$ . The propagation length is taken to be  $10\ \text{cm}$  when the power is  $30\ \text{kW}$  and  $0.6\ \text{cm}$  at  $500\ \text{kW}$ .



Fig. 2(a). The crossing of these latter curves with the unstable regions provides the GPI gain regions as a function of frequency. Clearly, as the input power is increased to 500 kW, the transition curves separating stable and unstable regions are significantly altered, in such a way that the unstable regions become wider [Fig. 2(a)], signifying broader frequency bands in which GPI can take place. On the other hand, for lower powers, this line is close to  $\rho \sim 0$  [black curve in Fig. 2(a)], and the GPI sidebands are considerably narrower and can thus be described via standard perturbative methods. However, this is not the case as the power increases where the Hill's equation needs to be formally treated, as done in Secs. II and III. In this regime, because of self-focusing effects, the higher-order harmonics in the Fourier series expansion of  $f(\xi)$ , resulting from more severe beam expansions/compressions, play an important role in determining the boundaries between stable and unstable domains in the stability diagram. The actual gain ( $\propto \mu$ ) of the GPI sidebands can also be directly obtained from Eq. (29). The GPI gain spectra are depicted in Fig. 2(b) as a function of frequency  $\Omega/2\pi$ , for 30 and 500 kW. Note that as the power increases, the GPI gain is considerably enhanced, while the peaks of the sidebands are shifted toward the pump wavelength. In addition, the spectral width of these GPI sidebands also increases with power. Again, this is a consequence of the large variations in spot size, as expected from the emergence of self-focusing effects. It is worth mentioning that the 500 kW level is quite below that for self-focusing collapse in bulk silica ( $\sim 3$  MW).

In order to numerically verify our analytical predictions, we accordingly performed a set of simulations using beam propagation methods. As suggested in Ref. 33, the  $(3+1)$ D problem of Eq. (1) can be approximately reduced to a  $(1+1)$ D NLSE after assuming a solution of the form  $\varphi(x, y, z, T) = u(z, T)G(x, y, z)$ , where the spatial beam profile  $G(x, y, z)$  was

taken again to be Gaussian. By doing so, the envelope  $u(z, T)$  is found to obey

$$i \frac{\partial u}{\partial z} + \sum_{n=2}^{\infty} \frac{i^n \beta_0^{(n)}}{n!} \frac{\partial^n u}{\partial T^n} + \frac{k_0 n_2 |A_0|^2 W_0^2}{2W^2(z)} |u|^2 u = 0, \quad (30)$$

where again  $W^2(z)$  is given by Eq. (16), which implicitly accounts for any possible self-focusing. The generated GPI sidebands, as predicted by Eq. (30), are provided in Fig. 2(c) as a function of frequency for both 30 and 500 kW. These numerical results are in excellent agreement with theoretical predictions based on Eqs. (27) and (29). The tendency for the sidebands to move toward the pump wavelength as the power increases is also evident in Fig. 2(c).

Finally, a series of experiments have been conducted in GRIN MMFs with different core radii. In our experiments, we used two different parabolic fibers having core diameters of 60  $\mu\text{m}$  and 80  $\mu\text{m}$ . The length of both fibers was  $\sim 5$  m. A Q-switched microchip laser was used at 1064 nm (400 ps, 95  $\mu\text{J}$ , and 500 Hz) with a peak power of  $\sim 185$  kW. Both fibers had a numerical aperture of NA = 0.2. For these parameters, the beam in these parabolic MMFs oscillates with a period of 0.666 mm for the 60  $\mu\text{m}$  diameter MMF and with a period of 0.888 mm for the 80  $\mu\text{m}$  diameter MMF. At this wavelength, the 60  $\mu\text{m}$  diameter fiber can support up to 313 modes (in both polarizations), while the 80  $\mu\text{m}$  diameter fiber can support up to 557 modes. Figure 3(a) shows the expected GPI gain spectra (using the results of Sec. III), corresponding to these two fibers at  $\sim 185$  kW. Similarly, Fig. 3(b) depicts the GPI gain as obtained from beam propagation methods, Eq. (30), for these fibers—in agreement with the gain peaks of Fig. 3(a). The measured GPI gain spectra from these two fibers are shown in Figs. 3(c) and 3(d) when the peak power is  $\sim 185$  kW. In both cases, we obtained good agreement between theory and

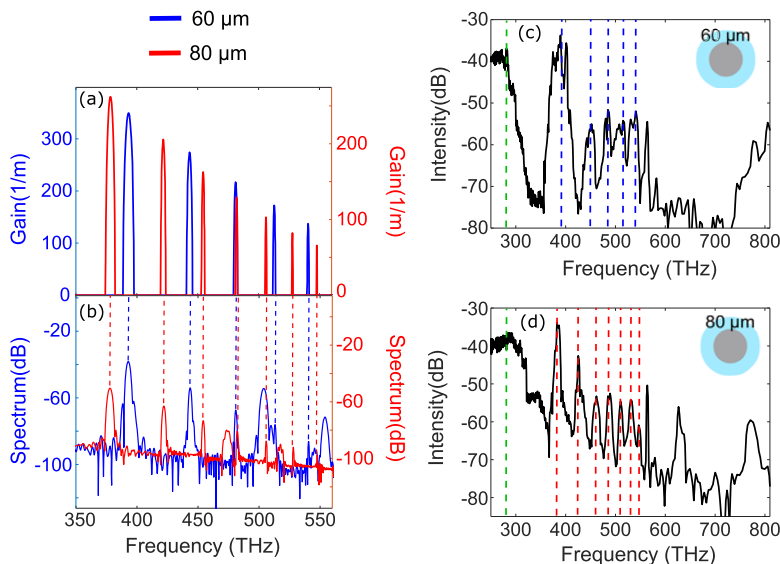


**FIG. 3.** GPI gain spectra as obtained from (a) analytical procedures and (b) numerical simulations in two different parabolic MMFs having core diameters of 60  $\mu\text{m}$  and 80  $\mu\text{m}$ . Experimentally measured GPI spectra from a  $\sim 5$  m long (c) 60  $\mu\text{m}$  core diameter MMF and (d) 80  $\mu\text{m}$ . In (a)–(d), the peak power was  $\sim 185$  kW. The green dotted lines indicate the pump frequency (1064 nm), while the blue (red) dotted lines correspond to the blue (red) GPI peaks, as predicted analytically in (a).

experiment concerning the actual positions of the GPI peaks. The shifting and widening of the GPI sidebands in the experimentally measured spectra of Figs. 3(c) and 3(d) are also in agreement with analytical predictions. Interestingly, as the core radius increases and hence the number of modes, the GPI sidebands experience a shift and become wider as predicted theoretically in the gain spectrum of Fig. 3(a) and corroborated by numerical simulations [Fig. 3(b)].

## V. CONCLUSION

In this work, we have presented a rigorous analysis of the GPI process in GRIN MMFs. Our approach is general and accounts for dispersion to all orders, as well as for high intensity conditions. The problem was effectively casted as a Hill's equation and was subsequently investigated using Floquet techniques. By doing so, we were able to obtain the corresponding stability diagrams and GPI gain spectra. Our results indicate a considerable change in the unstable regions, as the input power increases. Experimental results obtained from GRIN MMFs having different core radii corroborate our analytical predictions. Of interest will be to analyze similar problems based on the methodology presented in this paper. These may include, for example, the case where a Gaussian beam is launched off-axis (with or without angular momentum) or when an elliptic input beam is used—in which case the beam oscillation frequencies may be incommensurate. Our results could pave the way toward a better understanding of the GPI sideband generation and supercontinuum production in MMFs, especially at high power levels where perturbative schemes could be inapplicable.

## ACKNOWLEDGMENTS

This work was supported by the Office of Naval Research (ONR) (No. MURI N00014-17-1-2588), National Science Foundation (NSF) (No. ECCS-1711230), HEL-JTO (No. W911NF-12-1-0450), Army Research Office (ARO) (No. W911NF-12-1-0450), Air Force Office of Scientific Research (AFOSR) (No. FA955015-10041), and Qatar National Research Fund (QNRF) (No. NPRP9-020-1-006).

## REFERENCES

- <sup>1</sup>E. P. Ippen and R. H. Stolen, *Appl. Phys. Lett.* **21**, 539 (1972).
- <sup>2</sup>A. Hasegawa and F. Tappert, *Appl. Phys. Lett.* **23**, 142 (1973).
- <sup>3</sup>R. H. Stolen and C. Lin, *Phys. Rev. A* **17**, 1448 (1978).
- <sup>4</sup>L. F. Mollenauer, R. H. Stolen, and J. P. Gordon, *Phys. Rev. Lett.* **45**, 1095 (1980).
- <sup>5</sup>Y. Kodama and A. Hasegawa, *IEEE J. Quantum Electron.* **23**, 510 (1987).
- <sup>6</sup>K. Tai, A. Hasegawa, and N. Bekki, *Opt. Lett.* **13**, 392 (1988).
- <sup>7</sup>N. Akhmediev and M. Karlsson, *Phys. Rev. A* **51**, 2602 (1995).
- <sup>8</sup>S. Ramachandran, S. Ghalmi, J. W. Nicholson, M. F. Yan, P. Wisk, E. Monberg, and F. V. Dimarcello, *Opt. Lett.* **31**, 2532 (2006).
- <sup>9</sup>R. H. Stolen, *J. Lightwave Technol.* **26**, 1021 (2008).
- <sup>10</sup>G. P. Agrawal, *J. Opt. Soc. Am. B* **28**, A1 (2011).
- <sup>11</sup>P. Russell, *Science* **299**, 358 (2003).
- <sup>12</sup>J. C. Knight, *Nature* **424**, 847 (2003).
- <sup>13</sup>D. J. Richardson, J. M. Fini, and L. E. Nelson, *Nat. Photonics* **7**, 354 (2013).
- <sup>14</sup>A. Mafi, *J. Lightwave Technol.* **30**, 2803 (2012).
- <sup>15</sup>W. H. Renninger and F. W. Wise, *Nat. Commun.* **4**, 1719 (2013).
- <sup>16</sup>A. Picozzi, G. Millot, and S. Wabnitz, *Nat. Photonics* **9**, 289 (2015).
- <sup>17</sup>A. Gulistan, S. Ghosh, S. Ramachandran, and B. M. A. Rahman, *Opt. Express* **25**, 29714 (2017).
- <sup>18</sup>Z. S. Eznaveh, M. A. Eftekhar, J. E. A. Lopez, M. Kolesik, A. Schlzgen, F. W. Wise, D. N. Christodoulides, and R. A. Correa, *Opt. Lett.* **42**, 1015 (2017).
- <sup>19</sup>H. Pourbeyram and A. Mafi, *Opt. Lett.* **43**, 2018 (2018).
- <sup>20</sup>C. Mas Arab, A. Kudlinski, A. Mussot, and M. Conforti, *Phys. Rev. A* **97**, 023803 (2018).
- <sup>21</sup>L. G. Wright, D. N. Christodoulides, and F. W. Wise, *Nat. Photonics* **9**, 306 (2015).
- <sup>22</sup>L. G. Wright, S. Wabnitz, D. N. Christodoulides, and F. W. Wise, *Phys. Rev. Lett.* **115**, 223902 (2015).
- <sup>23</sup>L. G. Wright, W. H. Renninger, D. N. Christodoulides, and F. W. Wise, *Opt. Express* **23**, 3492 (2015).
- <sup>24</sup>K. Krupa, A. Tonello, B. M. Shalaby, M. Fabert, A. Barthlmy, G. Millot, S. Wabnitz, and V. Couderc, *Nat. Photonics* **11**, 237 (2017).
- <sup>25</sup>J. M. Dudley, F. Dias, M. Erkintalo, and G. Genty, *Nat. Photonics* **8**, 755 (2014).
- <sup>26</sup>L. G. Wright, D. N. Christodoulides, and F. W. Wise, *Science* **358**, 94 (2017).
- <sup>27</sup>S. Kawakami and J. Nishizawa, *IEEE Trans. Microwave Theory Tech.* **16**, 814 (1968).
- <sup>28</sup>D. Gloge and E. A. J. Marcatili, *Bell Syst. Tech. J.* **52**, 1563 (1973).
- <sup>29</sup>S. Longhi, *Opt. Lett.* **28**, 2363 (2003).
- <sup>30</sup>K. Krupa, A. Tonello, A. Barthlmy, V. Couderc, B. M. Shalaby, A. Bendahmane, G. Millot, and S. Wabnitz, *Phys. Rev. Lett.* **116**, 183901 (2016).
- <sup>31</sup>G. Lopez-Galmiche, Z. S. Eznaveh, M. A. Eftekhar, J. A. Lopez, L. G. Wright, F. Wise, D. Christodoulides, and R. A. Correa, *Opt. Lett.* **41**, 2553 (2016).
- <sup>32</sup>K. Krupa, C. Louot, V. Couderc, M. Fabert, R. Guenard, B. M. Shalaby, A. Tonello, D. Pagnoux, P. Leproux, A. Bendahmane, R. Dupiol, G. Millot, and S. Wabnitz, *Opt. Lett.* **41**, 5785 (2016).
- <sup>33</sup>M. Conforti, C. Mas Arabi, A. Mussot, and A. Kudlinski, *Opt. Lett.* **42**, 4004 (2017).
- <sup>34</sup>D. Anderson, *Phys. Rev. A* **27**, 3135 (1983).
- <sup>35</sup>M. Karlsson, D. Anderson, and M. Desaix, *Opt. Lett.* **17**, 22 (1992).
- <sup>36</sup>A. D. Polyanin and V. F. Zaitsev, *Handbook of Exact Solutions for Ordinary Differential Equations*, 2nd ed. (CRC Press, 2003).
- <sup>37</sup>L. P. Pitaevskii, *Phys. Lett. A* **221**, 14 (1996).
- <sup>38</sup>F. K. Abdullaev, S. A. Darmany, S. Bischoff, and M. P. Sørensen, *J. Opt. Soc. Am. B* **14**, 27 (1997).
- <sup>39</sup>D. W. Jordan and P. Smith, *Nonlinear Ordinary Differential Equations: An Introduction for Scientists and Engineers*, 4th ed. (Oxford University Press, 2007).
- <sup>40</sup>E. T. Whittaker and G. N. Watson, *A Course of Modern Analysis*, 4th ed. (Cambridge University Press, 1950).
- <sup>41</sup>G. P. Agrawal, *Nonlinear Fiber Optics*, 5th ed. (Academic Press, 2013).